

## STATISTICAL PROPERTIES OF SOLAR CORONAL BRIGHT POINTS

N. ALIPOUR AND H. SAFARI

Department of Physics, University of Zanjan, P.O. Box 45195-313, Zanjan, Iran; alipourrad@znu.ac.ir, safari@znu.ac.ir

Received 2014 July 22; accepted 2015 April 27; published 2015 July 9

## ABSTRACT

Here, we aim to study the statistical properties (i.e., spatial, temporal, and magnetic structures) of extreme ultraviolet coronal bright points (CBPs) observed by *SDO* during a 4.4 yr period (2010 June 1 to 2014 October 31). We developed the automatic detection method for CBPs based on the machine-learning technique and Zernike image moments. The average number and the mean density of CBPs are estimated to be about 572 (per full disk image taken at 193 Å) and  $1.9 \times 10^{-4} \text{ Mm}^{-2}$ , respectively. There is a negative correlation ( $-0.7$ ) between the number of CBPs and the number of sunspots. The size and lifetime frequency distribution of CBPs show the lognormal and power-law (exponent equal to  $-1.6$ ) behaviors, respectively. The relationship between the lifetime and size of CBPs is clearly treated by a power-law function with an exponent equal to 0.13. Around 1.3% of the solar surface is covered by the bright cores of CBPs and 2.6% of that is covered by their total area. About 52% of CBPs have lifetimes of less than 20 minutes and the remaining 48% have mean lifetimes of 6 hr. More than 95% of CBPs with lifetimes of less than 20 hr and nine CBPs with lifetimes of more than 72 hr are detected. The average number of the new CBPs emerging every 45 s in the whole of the Sun is about  $27 \pm 3$ . The temporal self-affinity of the time series of CBPs that emerged, indexed by the Hurst exponent determined using both detrended fluctuation analysis and *R/S* analysis, is 0.78. This long-temporal correlation suggests that CBPs form a system of self-organized criticality.

**Key words:** Sun: activity – Sun: corona – Sun: flares – Sun: magnetic fields – sunspots

**Supporting material:** animations

## 1. INTRODUCTION

Coronal bright points (CBPs) are the most ubiquitous features that have been observed in X-ray and extreme ultraviolet solar images (Vaiana et al. 1970, 1973; Golub et al. 1974; Habbal & Withbroe 1981). Generally, CBPs have sizes less than 60 arcsec and their lifetimes range from less than an hour to a few days (Vaiana et al. 1973; Zhang et al. 2001). 1500 X-ray bright points can emerge in a 24 hr period and are seen in quiet-Sun regions and coronal holes (Golub et al. 1976). CBPs display three types of morphological characteristics: point-like, small-loop, and small active regions (Sheeley & Golub 1979; Brajša et al. 2002). The majority of CBPs may be caused by the canceling of magnetic bipoles and a few percent of them are related to the emergence of magnetic flux (Webb et al. 1993; Parnell et al. 1994; Priest et al. 1994; Zhang et al. 2012). This suggests that most of the CBPs with opposite polarities lead to magnetic reconnection and therefore most likely play an important role in the local heating of the plasma.

Identification and tracking of CBPs derived from various solar data are the two key steps used to understand their physical and statistical properties. Various attempts have been undertaken: Brajša et al. (2002) investigated the detection technique of bright points in *Solar and Heliospheric Observatory* (*SOHO*)/EIT images; Hara & Nakakubo-Morimoto (2003) developed an automatic detection of bright points in *Yohkoh*/SXT images; and McIntosh & Gurnan (2005) proposed automatic detection and tracking of CBPs by using background intensity thresholds. Sattarov et al. (2010) investigated an automatic algorithm for the identification of CBPs in *SOHO*/EIT 193 Å images. Briefly, in their algorithm, the compact brightness regions that appeared above the active

regions are excluded from images with an intensity threshold based on a trial-and-errors process. The regions exceeding the area of a circle with a radius of 25 arcsec were labeled as active regions, and the potential CBPs within these areas were not considered. The closed contours with greater-than-average intensity were selected as potential CBPs. Additional criteria based on the intensity and morphological characteristics are used in selecting the CBPs.

To optimize the statistical analysis of various kinds of solar phenomena (e.g., flares, coronal mass ejections, mini-dimings, CBPs, etc.) observed by solar missions (e.g., *SDO*, *SOHO*, *Hinode*, *IRIS*, etc.), it is necessary to develop automatic detection techniques. Aschwanden (2010) gave an extensive overview of solar image processing techniques that are used in automated feature detection algorithms for small and large events.

Due to the fact that CBPs have often displayed very irregular variations in the X-ray and EUV intensities, here we apply automatic detection of CBPs to 193 Å *SDO*/AIA images based on the invariant Zernike moments and the Support Vector Machine (SVM) classifier. These invariant features allow us to detect CBPs by using the proposed method even if the events have been exposed to rotation, translation, and scaling. First, we computed the Zernike moments for series of CBPs and non-CBPs that were afterward fed into SVM as our training data set. For CBP tracking in consecutive images, the intersection of the regions of separate events are compared in their corresponding lifetimes.

In what follows, first an overview of data analysis is discussed in Section 2. The automatic identification and tracking algorithms will be proposed in Section 3. Then, statistical studies are illustrated in Section 4. Finally, a discussion and summary are presented in Section 5.

## 2. DATA PRE-PROCESSING

To study the statistical properties (number, filling factor, size, etc.) of CBPs we used the daily full disk images obtained from 2010 June 1 to 2014 October 31 at 193 Å AIA. Also, to study the statistical properties (lifetime, newly emerged CBPs, etc.) the data set used here consists of a sequence of full disk images obtained on two specific days, 2010 June 7 (day 1) and 2011 February 13 (day 2) with 45 s intervals at 193 Å AIA and the co-temporal line-of-sight magnetic field at 6173 Å HMI. To adapt the image pixel size with different filters to a common spatial resolution (0.6 arcsec), level 1.0 data were then converted to level 1.5. HMI data and were provided along with AIA data and re-scaled (AIA Plate-scale), rolled, and adjusted to the same AIA. To determine the position of CBPs automatically at the sequence of images, we corrected the solar differential rotation.

## 3. AUTOMATIC IDENTIFICATION AND TRACKING ALGORITHMS

CBP identification methods have been developed to capture intensity-based characteristics compared with the background and some additional criteria on shape and size (e.g., Sattarov et al. 2002, 2010; Hara & Nakakubo-Morimoto 2003; McIntosh & Gurman 2005). Using machine-learning method (SVM) in image processing, Alipour et al. (2012) developed an automatic method to detect solar mini-dimmings. First, they used Zernike moments to map the mini-dimmings observed in time-slice images onto the finite sets of complex numbers. Image moments can describe properties of an image such as intensity, centroid, orientation, and other information that lie in the morphological structure. Then, these sets are learned by an automatic network classifier (SVM) until the automatic detection process is completed. Javaherian et al. (2014) developed a similar method for identifying photospheric features (bright points and granules) from SUFI/Sunrise images. Here, this method is adopted for automatic identification and tracking of CBPs from *SDO* data. The following steps are employed to fulfill the automatic detection of CBPs taken by AIA at 193 Å.

### 1. CBPs are seen in the quiet-Sun regions and coronal holes.

For convenience, we probed (by eye) the data to collect a set of CBPs (rare and common). To do this, following Sattarov et al. (2010), we selected potential CBPs centered on an image tile with radius greater than 2 Mm (3'') and smaller than 20 Mm (28'') (size criterion). The bright features with sizes less than 2 Mm and lifetimes less than 45 s were called bright dots or nanoflares (Régner et al. 2014). The morphological structures of CBPs are point-like or small-loop-like. Their shapes would not be elongated and are also not crescent-like structures (parts of bright large coronal loops; shape criterion). Subramanian et al. (2010, 2012) show that the intensity of the EUV brightenings increase up to 1.3 times the background (intensity criteria). In Figure 1, the image tiles of a sample CBP and its light curve are presented from starting time (13:37 UT) to end time (14:20 UT). We see that the peak value of intensity is 2.5 times larger than the average intensity of image tiles (including the CBP and its surrounding). To make certain that the selected features are correctly CBPs, some additional criteria as explained by Chandrasekhar et al.

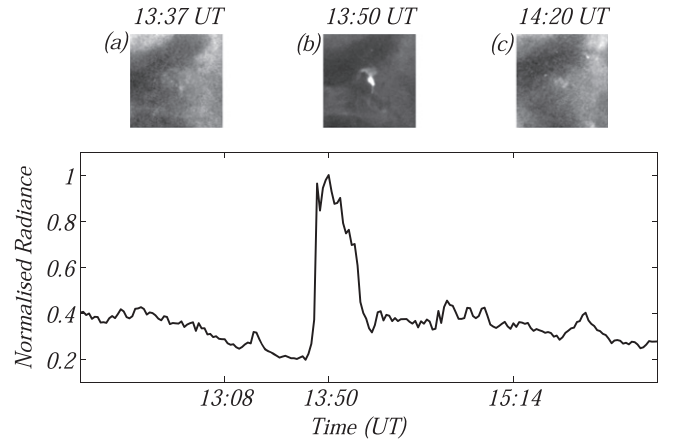


**Figure 1.** (Top) the image tiles of the CBP detected by *SDO*/AIA on 2011 February 13 (a) at the start time 13:37 UT, (b) at the peak time 13:50 UT, and (c) at the end time 14:20 UT. (Bottom) the normalized intensity profile (light curve) of the CBP is shown. The peak intensity is about twice that of the background.

(2013) are examined. They show that most CBPs appear in different channels of AIA (171, 193, and 211 Å) similar to small-scale active regions. So, co-spatial and co-temporal images (on channels of AIA 171, 193, and 211 Å) and HMI magnetograms confirm that the selected features are correctly CBPs. We note that often a CBP represents a set of small-scale magnetic loops connecting a bipolar region. When the bipolar region is more complex, then the CBP will appear more complex. The loops forming CBPs at different heights may have different temperatures, so the CBP will look slightly different in different AIA channels. Kwon et al. (2010), using a stereoscopic technique on *STEREO*/EUVI images, estimated the average height of CBPs above solar surface to be about 5 and 7 Mm for 171 and 195 Å, respectively. The magnetic polarity of CBPs (in HMI data) shows emerging and/or canceling within the bipole regions. The final collection of the selected CBPs (a set of 700 CBPs) is labeled class 1 of our training data set. Most of the selected CBPs have point-like, small-loop, and small multiple-loop shapes (Figure 2, first row). Some non-CBP features (part of large-loop regions, active regions, regions without considerable bright events, etc.) picked up at a size of 60'' × 60'' are labeled class 2 (Figure 2, second row).

2. The Zernike moments of the image tiles including CBP and non-CBP are computed. The magnitude values of the moments are fed to the SVM classifier. Now, our network classifier is ready to use.
3. Each  $N_i$  image of size 4096 × 4096 from AIA at 193 Å was calibrated and de-rotated. An image tile, starting from  $x_1 = 1$  and  $y_1 = 1$  with size  $\Delta x = 6''$  and  $\Delta y = 6''$  (small box), is extracted. The locations ( $x_{\max}$ ,  $y_{\max}$ ) of the maximum intensity inside this small region is determined. A larger image tile is selected around the maximum intensity position with size  $\Delta x = 60''$  and  $\Delta y = 60''$ . The Zernike moments of this image tile is computed and the magnitudes of the moments are fed to the classifier. The code picks up label 1 for a CBP feature and 2 for a non-CBP feature. If it is a CBP, the locations ( $x_{\max}$ ,  $y_{\max}$ )

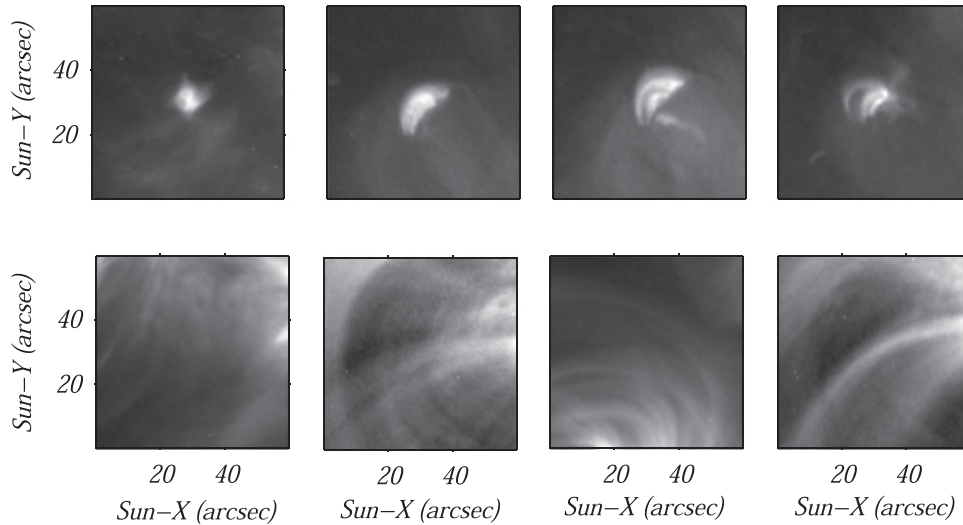


**Figure 2.** (Top row) samples of image tiles including CBPs with different shapes (point-like, small loop, small multiple loop, etc.) observed by *SDO/AIA* at 193 Å. (Bottom row) samples of image tiles including non-CBP features (parts of large-loop regions, active regions, etc.).

and time  $t$  are saved. Then the small box is moved first in the  $x$ -direction until the end of the grid is reached and then it is moved in the  $y$ -direction.

4. The CBPs recognized in each image that have distances from the brightness centers (the position of the maximum value of brightness) larger than 60 arcsec are considered “separate events.” For distances smaller than 60 arcsec, using the region growing function, the region ( $R$ ) pixels of the CBP are determined. We know that the regions of two CBPs (indicated by  $i$  and  $j$ ) with separate pixels,  $R_i \cap R_j = \emptyset$ , are considered to be “separate events.”
5. The separate events in the sequential 193 Å images with an intersection of regions are tracked. To do this, we organized the tracking algorithm in two semi-parallel parts. In the first part of the tracking algorithm, the positions of the separate events at times  $t_i$  ( $i$  is the image number) and  $t_{i+1}$  are compared and events with an intersection of regions are marked with the same labels. The separate events with the same labels and ignorable gaps in time are defined as “single events” (CBP). In the case of time gaps (probably because of missing images, bad images, or identification error) for two sequential images with a time distance larger than one cadence and for the same labels, the second part of the tracking algorithm is applied. In the second part, the co-temporal images at the 171 and 211 Å channels, on the same positions as a separate event, the identification algorithm is employed. If the code at least identified the CBP on one of these channels, then the time gap is added to the lifetime of the CBP; we also called these single events. Otherwise a new CBP is started. We see that in some cases that, (1) at least two or more CBPs are close together and merged (evolved CBP). In this case, we added the lifetime of an evolved CBP to that of a CBP with a maximum intersection of regions before merging; or (2) a CBP (main CBP) is fragmented into two or several CBPs (fragmented CBPs). The lifetime of one of the fragmented CBPs which has a maximum intersection with the region by the main CBP is added to the lifetime of the main CBP.

## 4. RESULTS

### 4.1. Separate Events

Using the automatic identification method, CBPs appeared in full disk images at 193 Å observed by *SDO/AIA*. In Figure 3, the sample of faint and small CBPs detected by the algorithm are presented. Javaherian et al. (2014) have shown that the structures of Zernike moments are distinctive enough to identify the faint and bright features with various sizes and different rotation angles using the SVM classifier. The inconsistency between the number of CBPs with previous studies may depend on the performances of recognition algorithms. Over the 4.4 yr period (2010 June 1 to 2014 October 31) into cycle 24 the number of CBPs (Figure 4, left), the number of sunspots (Figure 4, middle), and the number of flares (Figure 4, right) are presented. The daily numbers, indicated by yellow lines, connect binned values for 13 data points, shown by the black lines, and the smoothed line for the binned values are presented by the red lines. An average number of 572, with a range from 427 to 790 CBPs (separate events) per image, was detected. This average number is 1.5 times more than that reported by Sattarov et al. (2010) and Zhang et al. (2001). The density (number of CBPs on the area of the solar surface) ranged from  $1.39 \times 10^{-4}$  to  $2.56 \times 10^{-4} \text{ Mm}^{-2}$  with a mean value of  $1.9 \times 10^{-4} \text{ Mm}^{-2}$ . The number of sunspots (from the Solar Influence Data Analysis Center) increased from 2010 to 2014, but the number of flares (all types) fluctuated around an average value. There is a strong negative correlation ( $-0.72$ ) (Pearson) between the number of sunspots and the number of CBPs and a weak negative correlation ( $-0.2$ ) between the number of flares and CBPs.

### 4.2. CBP Filling Factor

To compute the areas of the CBPs we transformed full disk images to Lambert cylindrical equal-area projection maps. The size of the CBPs of the projected images (Lambert) is slightly larger than the full disk images (original). The unknown pixel values are computed by using the interpolation function. This simple interpolation generates and adds some aliasing spatial frequencies to the near limbs outside of  $\pm 60^\circ$  longitude and

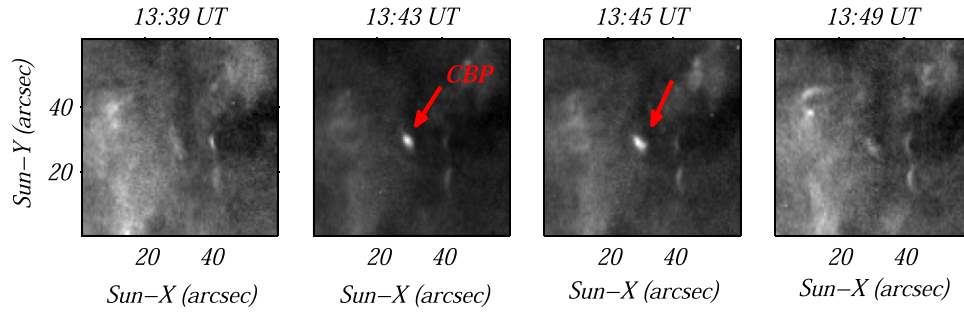


**Figure 3.** Image tiles of the faint and the small (with spatial diameter less than 7 arcsec) CBP with lifetimes less than 8 minutes detected by the present algorithm.

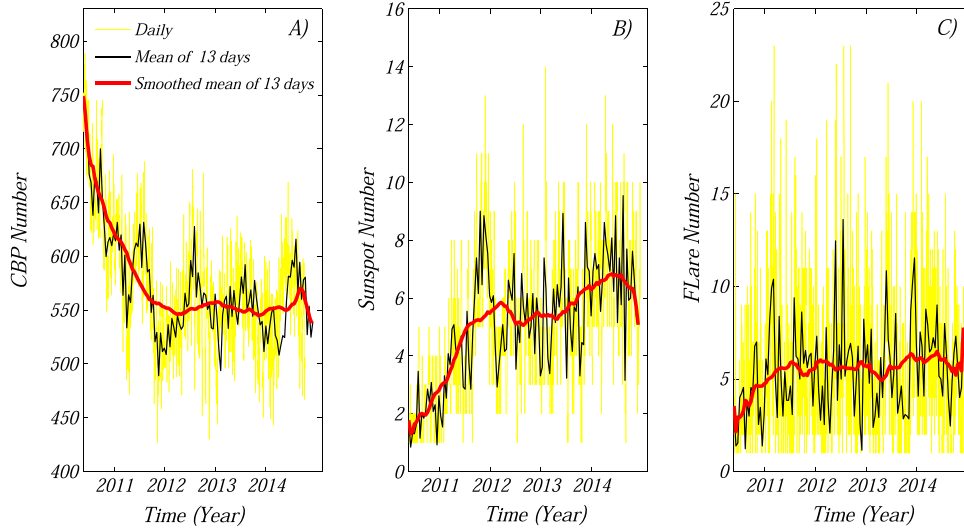


**Figure 4.** Number of CBPs (left), number of sunspots (middle), and number of all flare types (right) vs. time (daily from 2010–2014) are shown. The daily numbers (yellow lines), connected mean value of 13 days each (black lines), and smoothed mean of 13 days (red lines) are presented. A clear negative correlation of the number of sunspots to CBPs is shown (see text).

latitude from the disk center (e.g., DeForest 2004; McAteer et al. 2005). Therefore, we computed the areas of CBPs within  $\pm 60^\circ$  longitude and latitude.

The area ratio of the CBPs ( $R = A_{\text{Lambert}}/A_{\text{original}}$ ) of the projected maps ( $A_{\text{Lambert}}$ ) to the original images ( $A_{\text{original}}$ ) is calculated. The values of the ratios are categorized in three sets shown in Table 1. The area ratio of the CBPs bound to the solar equatorial regions (Figure 5, red contour lines; their longitudes and latitudes are given in region A of Table 1) is in the range of  $1 \leq R \leq 1.5$  and has a mean value of 1.3. This ratio for the CBPs located in the black contour lines (Figure 5 and region B of Table 1) holds within the interval of 1.5–2 with a mean value of 1.8. For the CBPs in the green contour lines (Figure 5 and region C of Table 1) the ratio range is 2–2.5 with a mean value of 2.3. Hereafter, in our analysis, we focused on the CBPs within  $\pm 60^\circ$  solar longitude and latitude.

Most CBPs emerge with a bright core (pixels with brightness larger than 50% of the maximum) and a halo (Figure 6). The mean values of the size of the bright cores and the total area of the CBPs are about 60 and 130  $\text{Mm}^2$ , respectively. Zhang et al. (2001) have estimated 110  $\text{Mm}^2$  on average for 41 CBPs in a region of size  $780'' \times 780''$ .

The size ( $A_{\text{CBP}}$ ) frequency distribution of the CBPs detected for a period of 4.4 yr is shown in Figure 7. The noisy the results in the tail (right-hand side) of the histogram depends on the statistical fluctuations larger than bin count numbers. It seems that this is normal for those events obeying a power-law

**Table 1**

The Area Ratio of CBPs  $R$  and its Mean Value  $\bar{R}$  in the Regions in Figure 5 vs. Solar Latitude  $\alpha$  and Longitude  $\phi$  in Heliographic Coordinates

Region: ( $\alpha, \phi$ )	$R$	$\bar{R}$
A: ( $ \alpha  < 15,  \phi  < 60$ ), ( $15 <  \alpha  < 30,  \phi  < 30$ ), ( $30 <  \alpha  < 40,  \phi  < 20$ )	[1 1.5]	1.3
C: ( $50 <  \alpha  < 60, 10 <  \phi  < 60$ ) ( $30 <  \alpha  < 40, 50 <  \phi  < 60$ ) ( $40 <  \alpha  < 60, 30 <  \phi  < 60$ )	[2 2.5]	2.3
B: Regions inside ( $ \alpha  < 60,  \phi  < 60$ ) and outside A and B	[1.5 2]	1.8

distribution with an exponent larger than 2 (Newman 2005). On the topic of bin widths, there is no best bin width, and different bin widths can show different distributions of data. Narrower bins give high density and the signal drowns the noise, while larger bin widths give low density and reduce noise. Several attempts were performed to obtain an appropriate or optimal number of bins without significant changes in the shape of the histogram (e.g., Venables & Ripley 2002). We used various rules to determine the optimal number of bins for our specific data. As shown in the figure, the tail of the distribution is skewed and a single power-law function is not



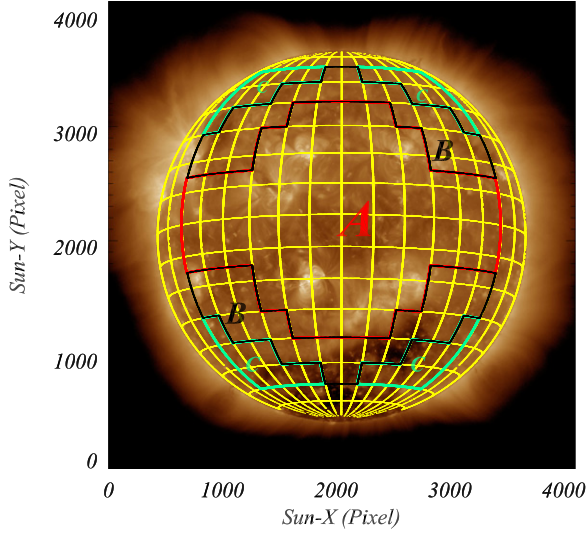


**Figure 5.** Solar surface within  $\pm 60^\circ$  longitude and latitude divided into three sub-regions based on the area ratio ( $R = A_{\text{Lambert}}/A_{\text{original}}$ ) of the CBPs: the mean value of the ratio is 1.3 for the solar equatorial regions as shown by the red contour lines (A); the mean value of the ratio is 1.8 for the regions with black contour lines (B); and the mean value of the ratio is 2.3 for the regions indicated by green contour lines (C). Longitudes and latitudes of each region are in Table 1.

(Animations (a, b, c and d) of this figure are available.)

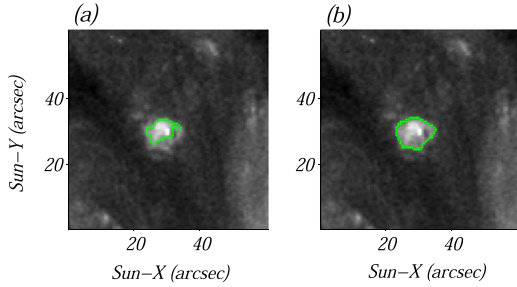


**Figure 6.** Demonstration of the CBP extracting from AIA images; (a) the bright core (region with brightness of larger than 50% of maximum), and (b) the total area.

well fitted to the histogram. The lognormal distribution function is a quadratic function in log scale,

$$y = -\frac{(\ln x)^2}{2\sigma^2} + \left(\frac{\mu}{\sigma^2} - 1\right) \ln x - \frac{\mu^2}{2\sigma^2}, \quad (1)$$

in which  $\mu$  and  $\sigma$  are the location and shape parameters. The fitted parameters are obtained as  $\sigma = 0.93$  (0.89–0.97) and  $\mu = 4.45$  (4.32–4.59), where the values of the brackets present the confidence bands with a 95% confidence level.

The filling factor of bright cores ( $A_{\text{BC}}$ ) for a full disk image is given by

$$f = \frac{\sum_{i=1}^N A_{\text{BC}}^i}{A_{\text{Sun}}}, \quad (2)$$

where  $N$  is the number of observed CBPs and  $A_{\text{Sun}}$  is the area of the solar surface within  $\pm 60^\circ$  longitude and latitude. The time series of the filling factor of bright cores and the curve-connected bins are shown in Figure 8. The filling factor is in the range of 0.009–0.017, and with mean values are 0.013. It

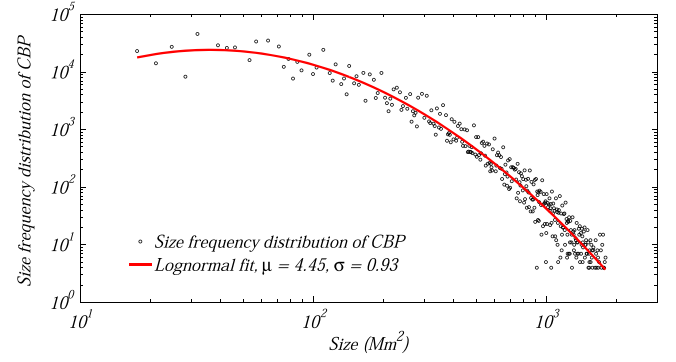


**Figure 7.** Size-frequency distribution of CBPs vs. size in log-log scale. The lognormal fit (indicated by the red line) is presented. The shape parameter ( $\sigma$ ) and location ( $\mu$ ) are 0.93 and 4.45, respectively (see text).

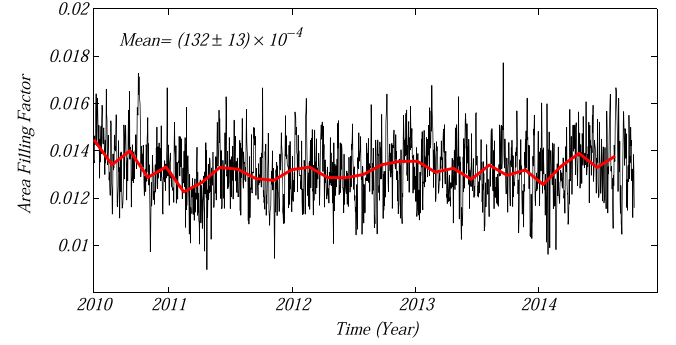


**Figure 8.** Time series of the area filling factor (total area covered by bright cores of CBPs, Equation (2)) for 2010 to 2014.

shows that around 1.3% of the solar surface is covered by the cores of CBPs. These findings are in agreement with Zhang et al. (2001). We note that the mean value of the total area of CBPs is roughly more than double that of the bright cores. This proves that 2.6% of the solar surface is covered by the total area of CBPs, a rate that is twice as much as previously reported.

#### 4.3. CBPs Tracking

Using an automatic tracking algorithm over the 21 hr period of both day 1 and day 2, the CBPs (within the region of  $\pm 60^\circ$  solar longitude and latitude) are tracked. The tracked CBPs are in one of following two cases: (a) the CBPs emerged and then disappeared during the day (day 1 or day 2) they were studied, or (b) the CBPs emerged in the day(s) before the day they were studied and/or disappeared in the day(s) after the day they were studied. For case (b), the identification and tracking algorithms are employed for the day(s) previous to (backward tracking) or the day(s) following (forward tracking) the day they were studied until the starting time or end time of such events is obtained. An example of a single event (CBP) with the lifetime less than 8 minutes (start time 13:41 UT and end time 13:49 UT) is shown in Figure 3. The lifetimes of detected CBPs are in the range of a few minutes to a few days. The CBPs with larger lifetimes ( $> 48$  hr) are rare and the code finds nine CBPs with lifetimes of more than 72 hr (Figure 9, labeled 1–9). The CBPs with label 1 and lifetimes of about 75 hr appear on 2011 February 11 04:20 UT to 2011 February 14 07:00 (movie-1). About 52% of the CBPs occurred with lifetimes less than 20 minutes with a mean value of 12 minutes

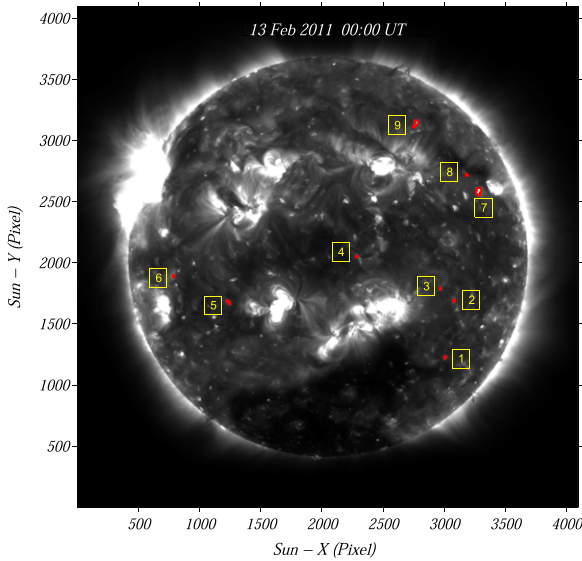


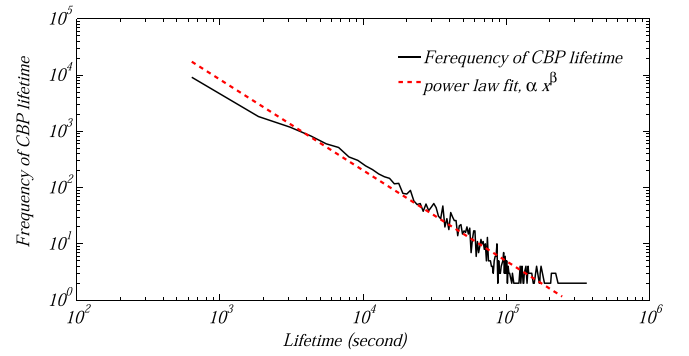
**Figure 9.** Location of nine CBPs (labeled by numbers 1–9) with lifetimes larger than 72 hr.

(transient events), and the rest (48%) have lifetimes of several hours with a mean value of 6 hr (persistent events). Wang et al. (1999) have shown that 90% of microflares are transient events. In Figure 10, the lifetime frequency distribution of CBPs is shown. We see that the fitted power-law exponent (slope of linear fit on log–log scale) is about  $-1.6$ . McIntosh & Gurman (2005) have shown that the frequency distribution of the CBP lifetime is a power law with exponential behavior for long lifetimes.

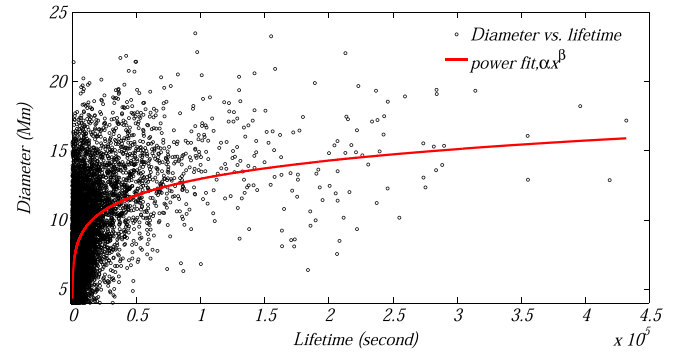
The relationship between lifetime ( $T$ ) and CBP size (mean value) is presented in a scatter plot (Figure 11). As we see in the scatter plot, (a) more than 95% of the CBPs have lifetimes less than 20 hr, and (b) CBPs with shorter lifetimes are more scattered in sizes, and with increasing CBP lifetimes their sizes are slightly increased (red line). The red line presents the power-law fit  $A_{\text{CBP}} = \alpha T^\beta$  with  $\alpha = 2.6$  (2.54–2.69) and  $\beta = 0.139$  (0.136–0.142) in which the values in brackets indicate the confidence bands with a 95% confidence level.

Figure 12 presents the number of the newly emerged CBPs as the time series for both day 1 (left) and day 2 (right). For both days, the average number of newly emerged CBPs is about 9 (standard deviation  $\sigma = 3$ ). The solar corona (i.e., quiet-Sun, coronal hole, etc.) is highly inhomogeneous in mass density, flow, and magnetic structures and is characterized by small-scale events. It seems that these inhomogeneities are related to the cellular patterns that constitute the networks and can be considered as complex systems concepts. Self-organized criticality (SOC) is one of the important concepts that can describe the complexity of nature. One may ask whether or not there are self-similarities or positive correlations (long-range dependencies) in the time series of newly emerged CBPs. Does the system of CBPs form a system of SOC? The intensity of the long-range dependence in a given time series can be estimated by the Hurst exponent (e.g., Weron 2002). Here, the  $R/S$  analysis and detrended fluctuation analysis (DFA) are used to estimate the self-similarity parameter  $H$ .

In  $R/S$  analysis, a time series ( $Z$ ) with length  $L$  is divided into  $M$  subwindows of length  $N$  ( $W_{i,j}$ ,  $j = 1, \dots, M$ ,  $i = 1, \dots, N$ ). For each subwindow, the average ( $A_j$ ) and



**Figure 10.** Lifetime-frequency distribution of CBPs (line) and linear fits (red line) in log–log scale. The power-law slope (slope of linear fit) is  $-1.6 \pm 0.07$ .



**Figure 11.** Relationship between CBP size ( $A_{\text{CBP}}$ ) and lifetime  $T$ . The power-law fit,  $A_{\text{CBP}} = \alpha T^\beta$  with  $\alpha = 2.6$  (2.54–2.69) and  $\beta = 0.139$  (0.136–0.142), is presented by the red line. The values in brackets indicate the confidence bands with a 95% confidence level, showing an interval estimate for the parameters of the fitted line.

standard deviation ( $S_j$ ) and the cumulative time series  $C_{i,j} = \sum_{k=1}^i (Z_{k,j} - A_j)$  are computed. Using the range value ( $R_j = \max\{C_{i,j}\} - \min\{C_{i,j}\}$ ,  $i = 1, \dots, N$ ), the normalized range to standard deviation  $R_j/S_j$  is computed. The average of the normalized range for  $N$  subwindows is given by  $(R/S)_N = \frac{1}{M} \sum_{j=1}^M \frac{R_j}{S_j}$ . Mandelbrot (1975) and Weron (2002) have shown that the  $R/S$  analysis shows asymptotic behavior as  $(R/S)_N \propto N^H$ , in which  $H$  is the Hurst exponent, and it can be obtained from a linear fit in log–log scale of  $(R/S)_N$  versus  $N$ .

In the DFA (Peng et al. 1994; Weron 2002) for each cumulative time series  $C_{i,j}$  a straight line  $\alpha_j x + \beta_j$  is fitted. The mean value of the mean square fluctuation for all subwindows is obtained using

$$F(N) = \frac{1}{M} \sum_{j=1}^M \left( \frac{1}{N} \sum_{i=1}^N (C_{i,j} - \alpha_j i - \beta_j)^2 \right)^{1/2}. \quad (3)$$

In a similar manner to  $R/S$  statistics, the Hurst exponent ( $H$ ) can be obtained by a linear fit (in log–log scale) for  $F(N)$  versus  $N$  (Weron 2002).

The values of  $0 < H < 0.5$ ,  $H = 0.5$ ,  $0.5 < H < 1$ ,  $H = 1$ , and  $H = 1.5$  indicate anti-correlated, uncorrelated, positive correlated, pink noise, and Brownian noise in the time series, respectively (e.g., Buldyrev et al. 1995). The values of the Hurst exponents are 0.84 and 0.84 ( $R/S$  analysis), and 0.75 and 0.77 (DFA) for the time series of newly emerged CBPs for day 1 and day 2, respectively (Figure 13). These values show long-

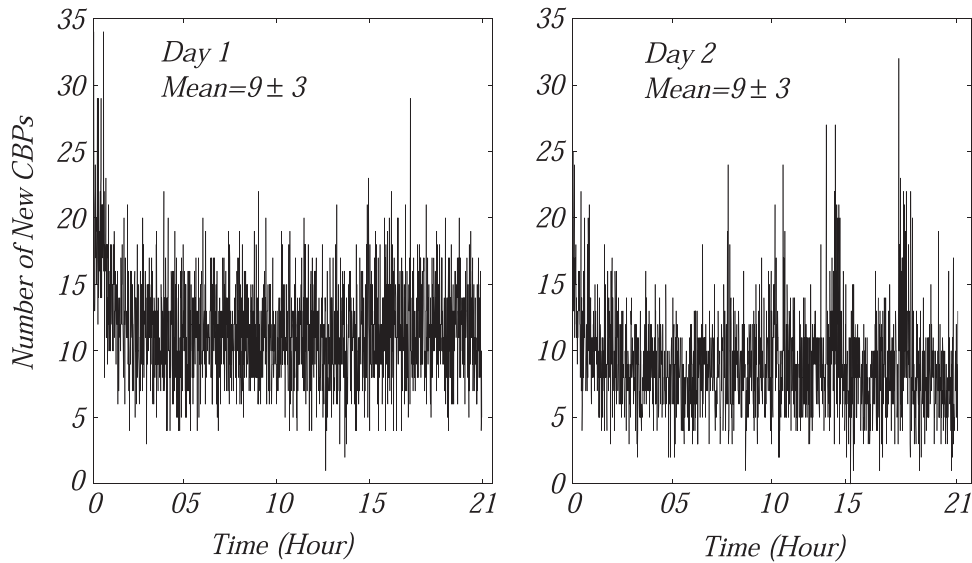


**Figure 12.** Number of new CBPs emerged in a time series for (left) day 1 (21 hr) and (right) day 2 (21 hr). The newly emerged CBPs within  $\pm 60$  solar longitudes and latitudes are considered.

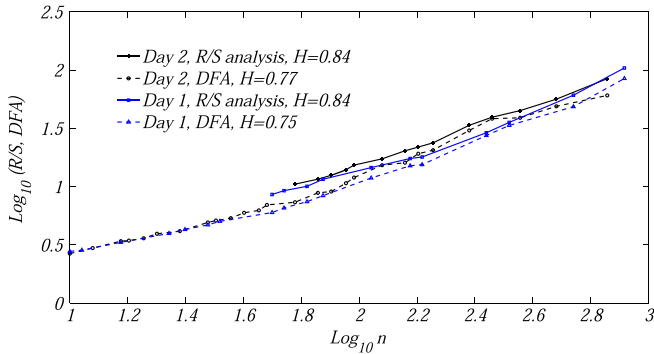


**Figure 13.** Applying detrended fluctuation analysis (DFA) and  $R/S$  analysis for time series of newly emerged CBPs (both day 1 and day 2), the Hurst exponent is determined. The average value of the Hurst exponent is about 0.78.

range dependencies (self-similarity) or positive correlations on the time series of newly emerged CBPs. This means that both a large number of newly emerged CBPs in the time series is most probably related to other large numbers and that numbers far into the future of the time series will also tend to be large. These values of the Hurst exponent (0.75–0.84) have shown a long-temporal correlation and suggest a system of SOC (see, e.g., Carreras et al. 2001; Dobson et al. 2007). Aschwanden et al. (2014) gave a review of SOC studies and its applications to solar physics and astrophysics and highlighted new trends, open questions, and future challenges. Zhang & Ji (2013) studied a system of three CBPs including a primary CBP and two sympathetic CBPs. They showed that the sympathetic CBPs emerged by thermal conduction arising from a primary CBP at a spatial distance of about 80 arcsec. The system of three CBPs is evidence of a self-organized system. More quantitative studies by (1) performing computational simulations on the coronal conditions of the formation of single CBPs and systems of CBPs and (2) testing several complex system models based on various networks (e.g., small worlds, regular network, random network, scale free, etc.) of CBP data are required to investigate the physical properties of systems of CBPs.

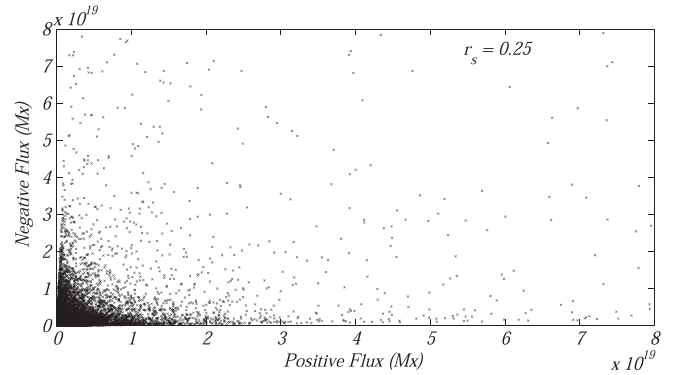


**Figure 14.** Scatter plot of negative ( $\Phi_-$ ) flux versus positive flux ( $\Phi_+$ ). The Spearman correlation coefficient is  $r_s = 0.25$ .

CBPs can be caused by two different magnetic mechanisms: emerging magnetic flux and canceling magnetic flux in chance encounters of opposite polarities (Priest 2014, p. 38). In the case of canceling magnetic flux, the opposite polarity magnetic fragments approach each other and then disappear. Their magnetic fluxes and fields are larger than the order of  $10^{17}$  Mx and 20 G, respectively. For CBPs (regardless of the lifetimes) located in region A the magnetic fragments above 20 G and below  $-20$  G are concerned. The Spearman correlation coefficient  $r_s$  between positive ( $\Phi_+$ ) and negative ( $\Phi_-$ ) magnetic fluxes are computed. According to Longcope et al. (2001), the coefficient is used to estimate the population percentage of CBPs caused by cancellation and/or emerging. A scatter plot of positive flux ( $\Phi_+$ ) versus negative flux ( $\Phi_-$ ) is shown in Figure 14. The correlation coefficient  $r_s = 0.25$  is interpreted to be 75% of the CBPs caused by canceling and the remaining 25% is due to the emerging bipoles (Webb et al. 1993).

## 5. DISCUSSION AND SUMMERY

In this paper, we proposed an algorithm for automatic identification (first step) and tracking (second step) of the CBPs and applied it to the AIA full disk images at 193 Å. In the

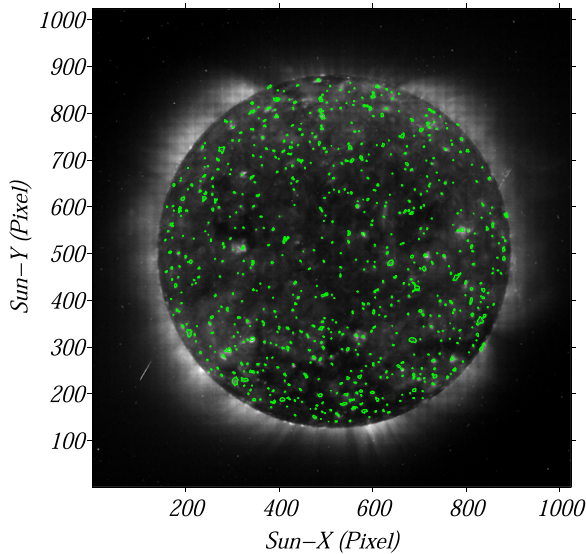


**Figure 15.** *SOHO*/EIT full disk image at 195 Å on 2008 February 16 00:00 UT. The locations of 670 CBPs (green contours) recognized by the presented algorithm are shown.

first step, the invariant Zernike moments of image tiles consisting of selected CBPs were fed into the SVM classifier. In order to compare the performance of the present identification method and previous methods, the following items are considered:

1. The aims of previous methods (e.g., Sattarov et al. 2010) for the identification of CBPs from solar images used the intensity thresholds (mean of intensity and its standard deviation of the full disk image in which the active regions were removed). The values of these thresholds depend on the background and noise of the images and the determination of unique and/or exact intervals is difficult.
2. The reliability of the present algorithm and similar ones as organized based on statistical machine-learning methods depends on the training process. We used the 1400 CBPs as the training set. This ensures that the classifier is tested on both common and rare (e.g., small

and faint) types of CBPs. To estimate the accuracy of the algorithm for the identification of CBPs, we selected (randomly) 400 CBPs and then found that only one case lacked the clear properties used in the training set (Section 3). In Figure 15, 670 detected CBPs on 2008 February 16 00:00 UT *SOHO*/EIT are shown. The previous study reported a maximum number of 450 CBPs detected based on their algorithm, for EIT images. For the period of our study (2010 June 1 to 2014 October 31), the average number of 500 CBPs per image on *SOHO*/EIT is obtained. There is about an 8% difference between the number of CBPs identified from *SDO*/AIA and *SOHO*/EIT at 193 Å. It seems that the spatial resolution of the instrument has effects on tiny events and may be smoothed and missed for low-resolution data.

In the second step, the intersection of the regions of the separate events in consecutive images was compared for the purpose of CBP tracking. The accuracy of our tracking algorithm highly depends on the cadence of the images and the distance of the neighboring CBPs. Consequently, the lifetimes of CBPs, their appearance in sequence images, and their disappearance are very sensitive to the accuracy of the tracking algorithm. In previous studies (e.g., Zhang et al. 2001), an average lifetime of CBPs of about 20 hr on *SOHO*/EIT data is reported. Using examples we show that the main cause of this discrepancy is related to differences of cadences of *SDO*/AIA (about 45 s as used here) and *SOHO*/EIT (about 26 minutes). Figure 16 presents the light curves (top) of the profile of the intensity and magnetic flux (bottom) of 12 CBPs that appeared successively in the small region (identified and tracked by the algorithm). We see that the photospheric magnetic fluxes of CBPs are significantly correlated with the co-temporal and co-spatial EUV emissions (see movie 2). As shown in the figure, CBP4 has overlapping times with CBP3 and it appears in the closed region (distance of brightness centers  $<10''$ ). Lifetimes of the 12 CBPs (see movie 3, with a cadence of 45 s) are in the range of 2–351 minutes and when we used a cadence of 26 minutes (movie 3), we saw only a single CBP with a lifetime of about 20 hr. In this case, because of their small lifetimes ( $<26$  minutes), CBP11 and CBP12 were not seen in movie 4.

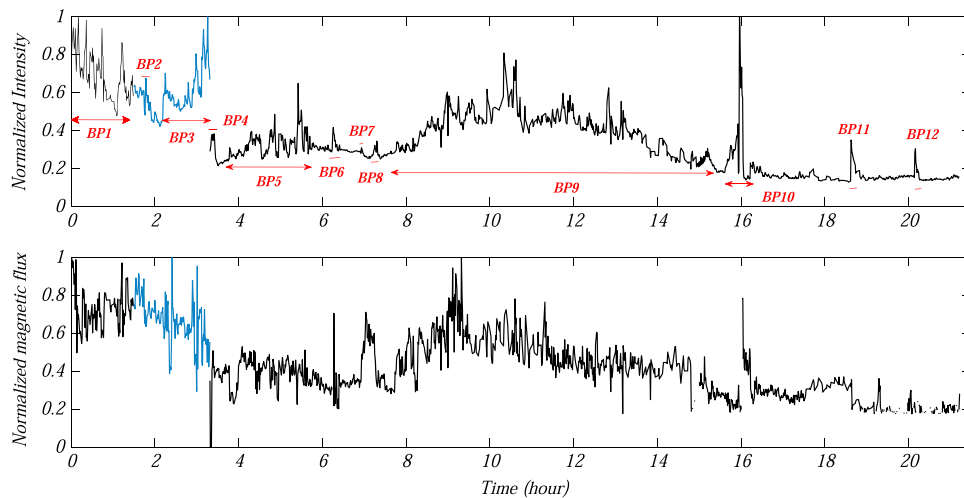


**Figure 16.** (Top) normalized absolute intensity profile and (bottom) correspondence absolute magnetic flux time series of 12 CBPs. All of these CBPs appeared within a small region. The overlapping times (03:18 UT) of CBP3 and CBP4 are clearly shown.

(Animations a, b and c of this figure are available.)



Zhang et al. (2001) raised a question regarding the relationship between transient brightenings of CBPs, and the long-term evolution of CBPs, but they could not answer this question because of the long cadence of their data set.

The summary of main results are listed here:

1. The average number of 579 CBPs per AIA image at 193 Å was detected. The average density, the number of CBPs on the solar surface area, is about  $1.9 \times 10^{-4} \text{ Mm}^{-2}$ .
2. Over the period of 4.4 yr (2010 June 1 to 2014 October 31) the number of sunspots and number of CBPs are clearly in opposite phases with a correlation coefficient of about  $-0.7$ .
3. The area ratio (Lambert cylindrical equal-area projection maps to full disk images) of CBPs (bounded on the solar equatorial regions) is about 1.3 (Table 1).
4. Most of the CBPs have a bright core and a halo. The mean value of the size of the bright cores and the total area of CBPs are about 60 and  $130 \text{ Mm}^2$ , respectively. The size–frequency distribution of the CBPs is treated in a lognormal function.
5. About 1.4% of the solar surface is covered by cores of CBPs, a finding that is consistent with Zhang et al. (2001).
6. More the 95% of the CBPs have lifetimes less than 20 hr. The identification and tracking code finds nine CBPs with lifetimes larger than 72 hr. The lifetime frequency distribution of CBPs is in power-law regions with a power index about  $-1.6$ .
7. The relationship between the CBP size and lifetime displays a power-law behavior,  $A \propto T^{0.13}$ . The CBPs with the smaller lifetimes are more scattered in size.
8. The average number of newly emerged CBPs within  $\pm 60^\circ$  solar longitude and latitude is about 9, for each 45 s. The CBPs that appeared in the regions outside of  $\pm 60^\circ$  solar longitude and latitude because of large area ratio ( $R = A_{\text{Lambert}}/A_{\text{original}}$ ) and their disappearance relative to solar rotation are not considered in these statistics. The total number of newly emerged CBPs (for each 45 s) in the whole solar corona at 193 Å emission are estimated to be about  $27 \pm 3$ .
9. The temporal self-affinity of new CBPs indexed by a Hurst exponent is about 0.75. The long-temporal correlation suggests that CBPs form an SOC system.

The authors thank the anonymous referee for very helpful comments and suggestions.

## REFERENCES

- Alipour, N., Safari, H., & Innes, D. E. 2012, *ApJ*, **746**, 12
- Aschwanden, M. J. 2010, *SoPh*, **262**, 235
- Aschwanden, M. J., Crosby, N., Dimitropoulou, M., et al. 2014, *SSRv*, in press
- Brajša, R., Wöhl, H., Vršnak, B., et al. 2002, *A&A*, **392**, 329
- Buldyrev, S. V., Goldberger, A. L., Havlin, S., et al. 1995, *PhRvE*, **51**, 5084
- Carreras, B. A., Newman, D. E., Dobson, I., & Poole, A. B. 2001, in Proc. 34th Hawaii Int. Conf. on System Sciences [http://www.hicss.hawaii.edu/HICSS\\_34/PDFs/CSSOC01.pdf](http://www.hicss.hawaii.edu/HICSS_34/PDFs/CSSOC01.pdf)
- Chandrasekhar, K., Prasad, S. K., Banerjee, D., et al. 2013, *SoPh*, **286**, 125
- DeForest, C. E. 2004, *SoPh*, **219**, 3
- Dobson, I., Carreras, B. A., Lynch, V. E., & Newman, D. E. 2007, *Chaos*, **17**, 026103
- Golub, L., Krieger, A. S., Silk, J. K., Timothy, A. F., & Vaiana, G. S. 1974, *ApJ*, **189**, 93
- Golub, L., Krieger, A. S., & Vaiana, G. S. 1976, *SoPh*, **49**, 79
- Habbal, S. R., & Withbroe, G. L. 1981, *SoPh*, **69**, 77
- Hara, H., & Nakakubo-Morimoto, K. 2003, *ApJ*, **589**, 1062
- Javaherian, M., Safari, H., Amiri, A., & Ziaei, S. 2014, *SoPh*, **289**, 3969
- Kwon, R. Y., Chae, J., & Zhang, J. 2010, *ApJ*, **714**, 130
- Longcope, D. W., Kankelborg, C. C., Nelson, J. L., & Pevtsov, A. A. 2001, *ApJ*, **553**, 429
- Mandelbrot, B. B. 1975, *Zeit. Wahrsch. verwandte Gebiet*, **31**, 271
- McAteer, R. T. J., Gallagher, P. T., Ireland, J., & Young, C. A. 2005, *SoPh*, **228**, 55
- McIntosh, S. W., & Gurman, J. B. 2005, *SoPh*, **228**, 285
- Newman, M. E. J. 2005, *ConPh*, **46**, 323
- Parnell, C. E., Priest, E. R., & Golub, L. 1994, *SoPh*, **151**, 57
- Peng, C. K., Buldyrev, S. V., Havlin, S., et al. 1994, *PhRvE*, **149**, 1685
- Priest, E. R. 2014, *Magnetohydrodynamics of the Sun* (Cambridge, UK: Cambridge Univ. Press), 38
- Priest, E. R., Parnell, C. E., & Martin, S. F. 1994, *ApJ*, **427**, 459
- Régnier, S., Alexander, C. E., Walsh, R. W., et al. 2014, *ApJ*, **784**, 134
- Sattarov, I., Pevtsov, A. A., Hojaev, A. S., & Sherdonov, C. T. 2002, *ApJ*, **564**, 1042
- Sattarov, I., Pevtsov, A. A., Karachik, N. V., Sherdanov, C. T., & Tillaboev, A. M. 2010, *SoPh*, **262**, 321
- Sheeley, N. R., Jr., & Golub, L. 1979, *SoPh*, **63**, 119
- Subramanian, S., Madjarska, M. S., & Doyle, J. G. 2010, *A&A*, **516**, 50
- Subramanian, S., Madjarska, M. S., Doyle, J. G., & Bewsher, D. 2012, *A&A*, **538**, 50
- Vaiana, G. S., Davis, J. M., Giacconi, R., et al. 1973, *ApJL*, **185**, 47
- Vaiana, G. S., Krieger, A. S., Van Speybroeck, L. P., & Zehnpfening, T. 1970, *BAPS*, **15**, 611
- Venables, W. N., & Ripley, B. D. 2002, *Modern Applied Statistics with S* (4th ed.; Berlin: Springer)
- Wang, H., Chae, J., Qiu, J., Lee, C., & Goode, P. R. 1999, *SoPh*, **188**, 365
- Webb, D. F., Martin, S. F., Moses, D., & Harvey, J. W. 1993, *SoPh*, **144**, 15
- Weron, R. 2002, *PhyA*, **312**, 285
- Zhang, J., Kundu, M. R., & White, S. M. 2001, *SoPh*, **198**, 347
- Zhang, Q. M., Chen, P. F., Guo, Y., Fang, C., & Ding, M. D. 2012, *ApJ*, **746**, 19
- Zhang, Q. M., & Ji, H. S. 2013, *A&A*, **557**, L5